X-ray spectroscopic study of BaFeO_{3} thin films: An Fe^{4+} ferromagnetic insulator

T. Tsuyama, T. Matsuda, S. Chakraverty, J. Okamoto, E. Ikenaga, A. Tanaka, T. Mizokawa, H. Y. Hwang, Y. Tokura, and H. Wadati

X-ray spectroscopic study of BaFeO$_3$ thin films; an Fe^{4+} ferromagnetic insulator

T. Tsuyama,[1] T. Matsuda,[1] S. Chakraverty,[2,3] J. Okamoto,[4]
E. Ikenaga,[5] A. Tanaka,[6] T. Mizokawa,[7] H. Y. Hwang,[2,8,9] Y. Tokura,[1,2] and H. Wadati[1]

[1]*Department of Applied Physics and Quantum-Phase Electronics Center (QPEC),*
University of Tokyo, Tokyo 113-8656, Japan.
[2]*RIKEN Center for Emergent Matter Science (CEMS), Wako 351-0198 Japan.*
[3]*Institute of Nano Science and Technology, Phase - 10, Sector - 64, Mohali, Punjab India.*
[4]*Condensed Matter Research Center and Photon Factory, Institute of Materials Structure Science (IMSS),*
High Energy Accelerator Research Organization (KEK), Ibaraki 305-0801, Japan.
[5]*Japan Synchrotron Radiation Research Institute (JASRI)/SPring-8, Kouto 679-5198, Japan.*
[6]*Department of Quantum Matter, ADSM, Hiroshima University, Higashi-Hiroshima 739-8530, Japan.*
[7]*Department of Complexity Science and Engineering, University of Tokyo, Chiba 277-8561, Japan.*
[8]*Stanford Institute for Materials and Energy Sciences,*
SLAC National Accelerator Laboratory, Menlo Park, CA 94025, USA.
[9]*Department of Applied Physics, Stanford University, Stanford, CA 94305, USA.*
(Dated: January 13, 2015)

We investigated the electronic and magnetic properties of fully oxidized BaFeO$_3$ thin films, which show ferromagnetic-insulating properties with cubic crystal structure, by hard x-ray photoemission spectroscopy (HAXPES), x-ray absorption spectroscopy (XAS) and soft x-ray magnetic circular dichroism (XMCD). We analyzed the results with configuration-interaction (CI) cluster-model calculations for Fe^{4+}, which showed good agreement with the experimental results. We also studied SrFeO$_3$ thin films, which have an Fe^{4+} ion helical magnetism in cubic crystal structure, but are metallic at all temperatures. We found that BaFeO$_3$ thin films are insulating with large magnetization ($1.7\mu_B/formula\ unit$) under $\sim$ 1 T, using valence-band HAXPES and Fe $2p$ XMCD, which is consistent with the previously reported resistivity and magnetization measurements. Although Fe $2p$ core-level HAXPES and Fe $2p$ XAS spectra of BaFeO$_3$ and SrFeO$_3$ thin films are quite similar, we compared the insulating BaFeO$_3$ to metallic SrFeO$_3$ thin films with valence-band HAXPES. The CI cluster-model analysis indicates that the ground state of BaFeO$_3$ is dominated by $d^5\underline{L}$ ($\underline{L}$: ligand hole) configuration due to the negative charge transfer energy, and that the band gap has significant O $2p$ character. We revealed that the differences of the electronic and magnetic properties between BaFeO$_3$ and SrFeO$_3$ arise from the differences in their lattice constants, through affecting the strength of hybridization and bandwidth.

PACS numbers:

I. INTRODUCTION

Strongly correlated transition-metal oxides show interesting physical properties such as colossal magnetoresistance, metal-insulator transitions, and the ordering of charge, orbital and spin [1]. Among this class of materials, high-valent metal compounds, such as SrFeO$_3$ and CaFeO$_3$, have attracted great attention due to their rich and anomalous physical properties. [2–11]. CaFeO$_3$ shows charge ordering below 290 K with the charge disproportion of $d^5\underline{L} + d^5\underline{L}$ $\longrightarrow d^5 + d^5\underline{L}^2$ ($\underline{L}$: ligand hole), inducing monoclinic crystal distortion [3–5]. The ground state of SrFeO$_3$ is dominated by the $d^5\underline{L}$ configuration and is metallic with cubic crystal structure. The $d^5\underline{L}$ electronic configuration gives rise to features in SrFeO$_3$, such as the helicoidal magnetic order, metallicity and absence of Jahn-Teller effect, which cannot be expected in the d^4 electronic configuration [9–13]. Mostovoy theoretically revealed that the helicoidal magnetic order of perovskite Fe^{4+} compound is attributed to the O $2p$ hole, rather than the competition between ferromagnetic double-exchange and antiferromagnetic superexchange interaction[12]. Furthermore, the reports of topological Hall effect suggest many possibilities for complex spin textures [7, 8].

BaFeO$_3$ is also one of those Fe^{4+} series, and Hayashi *et al.* reported the first success in synthesis of polycrystalline cubic BaFeO$_3$ with the lattice constant of 3.97 Å [14]. A-type helicoidal magnetic state with $\boldsymbol{q} = (0\ 0\ 0.06)\frac{2\pi}{a}$ ($a = 3.97$ Å) was found, but it becomes ferromagnetic under a small magnetic field of $\sim$ 0.3 T with a saturation magnetization of 3.5 $\mu_B/formula\ unit$ ($f.u.$), and transition temperature of 111 K, respectively [14]. Li *et al.* theoretically showed that the energy difference between the A-type helicoidal magnetic and ferromagnetic phase is quite small, and can be switched by small magnetic field in BaFeO$_3$ unlike SrFeO$_3$ [15, 16]. The difference in their magnetic properties is explained by the difference in their lattice constant: the larger Ba stretches out the lattice and decreases the strength of Fe $3d$ - O $2p$ hybridization, which closely relates to the magnetic phases [12, 15, 16].

There have been several reports on BaFeO$_3$ thin films on SrTiO$_3$ (001) substrates prior to the successful fabrication of bulk BaFeO$_3$, but all of them showed much lower magnetization and larger lattice constant than bulk BaFeO$_3$, due to oxygen vacancies in the thin films [17–20]. Chakraverty *et al.* reported the synthesis of fully oxidized single crystalline BaFeO$_3$ thin film which shows large saturation magnetization (in-plane; 3.2$\mu_B/f.u.$, out-of-plane; 2.7 $\mu_B/f.u.$) with the bulk lattice constant of 3.97 Å in cubic crystal structure [21]. Although the saturation magnetization and lattice constant of the recently reported thin film were quite close to that of bulk BaFeO$_3$, no signature of helicoidal magnetic structure has been observed [14, 21]. Transport and optical properties indicate that the fully oxidized film is an insulator with band gap $\sim$ 1.8 eV. The absence of the helicoidal magnetic order in BaFeO$_3$ film is likely due to the small energy barrier between the A-type helicoidal magnetic and the ferromagnetic phases, so that residual strain, or reduced dimensionality, stabilizes the uniform ferromagnet [16].

Given these exciting preliminary results on newly available single crystalline BaFeO$_3$ films, spectroscopic studies of the electronic and magnetic structures would be invaluable. For this purpose, we carried out hard x-ray photoemission spectroscopy (HAXPES) for Fe 2p core level and valence band, Fe 2p and O 1s x-ray absorption spectroscopy (XAS) and x-ray magnetic circular dichroism (XMCD). The results were analyzed with configuration-interaction (CI) cluster-model calculations. These experimental and calculated results accurately explain that the difference of the valence-band spectra between BaFeO$_3$ and SrFeO$_3$ originates from the differences in their strength of Fe 3d - O 2p hybridization due to the difference in their atomic distances (R) [the atomic distance of BaFeO$_3$ (R_{BFO}) is $\sim$ 1.99 Å and that of SrFeO$_3$ (R_{SFO}) is $\sim$ 1.93 Å, respectively].

II. EXPERIMENTAL AND CALCULATIONS

A single crystalline, cubic, fully oxidized 50 nm thin film of BaFeO$_3$ (with lattice constant 3.97 Å) was grown on SrTiO$_3$ (001) substrate, using pulsed laser deposition. The details of fabrication are described in Ref. [21]. HAXPES measurements were performed at BL47XU in SPring-8 at room temperature with the photon energy of 7940 eV (probing depth is $\sim$ 5 nm) [22] for both BaFeO$_3$ thin films and 50 nm thin films of SrFeO$_3$ on (LaAlO$_3$)$_{0.3}$-(SrAl$_{0.5}$Ta$_{0.5}$O$_3$)$_{0.7}$ (LSAT) (001) substrates to compare their electronic states [8]. The Fermi energy (E_F) position and the energy resolution of $\sim$ 250 meV were determined by measuring the Fermi edge of gold which has electrical contact with the samples. XAS and XMCD were carried out at BL-16A in Photon Factory at a temperature of 20 K. The magnetic field of $\sim$ 1 T was applied perpendicular to the thin film surface, strong enough to saturate the out-of-plane magnetization [21]. XMCD was measured by switching the applied magnetic field under a fixed circular polarization of the incident beam incident on the sample perpendicular to its plane. The probing depths of XAS and XMCD spectra are estimated to 1-5 nm [23–25]. The probing depths of HAXPES, XAS and XMCD are smaller than the film thickness (50 nm), making the obtained spectra affected by possible surface effects.

The CI cluster-model calculation has been prevalently utilized to describe the physical properties of correlated materials since it can treat the electronic correlation in a cluster precisely [1, 10, 26, 27]. The details of the CI cluster-model calculations are given in Refs. [10, 26, 27]. In this model, multiplet states including the charge transfer from oxygen ions to the iron ion are considered for a single octahedral [FeO$_6$]$^{8-}$ cluster. The wave function for the ground state (Ψ_i, Eq. (1)) and for the final state of Fe 2p core-level HAXPES (Ψ_{f_1}, Eq. (2)), of valence-band HAXPES (Ψ_{f_2}, Eq. (3)) and of Fe 2p XAS (Ψ_{f_3}, Eq. (4)) are described as

$$| \Psi_i \rangle = \alpha_1 | d^4 \rangle + \alpha_2 | d^5 \underline{L} \rangle + \alpha_3 | d^6 \underline{L}^2 \rangle + \cdots \tag{1}$$

$$| \Psi_{f_1} \rangle = \beta_1 | \underline{c} d^4 \rangle + \beta_2 | \underline{c} d^5 \underline{L} \rangle + \beta_3 | \underline{c} d^6 \underline{L}^2 \rangle + \cdots \tag{2}$$

$$| \Psi_{f_2} \rangle = \gamma_1 | d^3 \rangle + \gamma_2 | d^4 \underline{L} \rangle + \gamma_3 | d^5 \underline{L}^2 \rangle + \cdots \tag{3}$$

$$| \Psi_{f_3} \rangle = \delta_1 | \underline{c} d^5 \rangle + \delta_2 | \underline{c} d^6 \underline{L} \rangle + \delta_3 | \underline{c} d^7 \underline{L}^2 \rangle + \cdots \tag{4}$$

respectively. Here, $\underline{c}$ denotes the Fe 2p core hole. Fitting parameters in this model are the charge transfer energy from the O 2p orbitals to the empty Fe 3d orbitals denoted by Δ, the strength of Fe 3d - O 2p hybridization denoted by Slater-Koster parameters ($pd\sigma$), the on-site 3d - 3d Coulomb interaction energy denoted by U_{dd}. The parameters used in this work are summarized in TABLE I which were adjusted near the phase boundary of A-type helicoidal magnetic and ferromagnetic phases to explain the magnetic ground state of BaFeO$_3$ thin films [12]. The CI cluster-model calculation with our set of parameters revealed that the ground state is dominated by $d^5\underline{L}$ configuration (17 % d^4, 65 % $d^5\underline{L}$, 18 % $d^6\underline{L}^2$) due to the negative charge transfer energy.
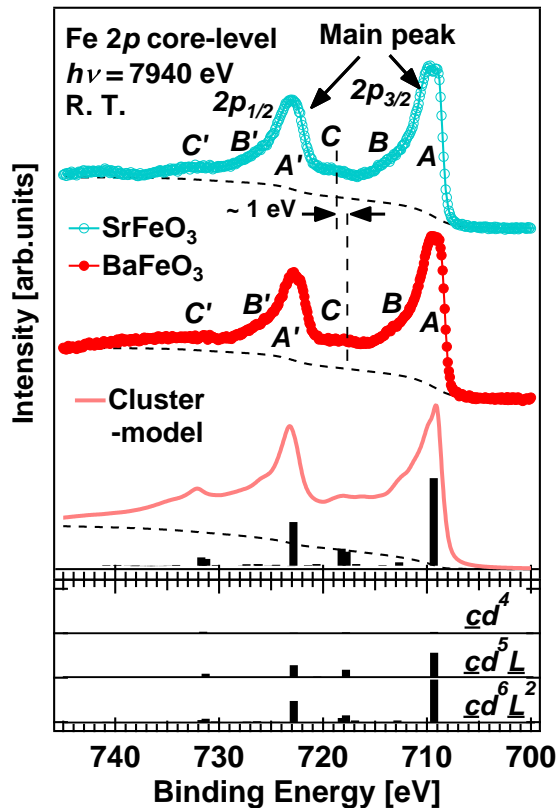
FIG. 1: (Color online) Fe $2p$ core-level HAXPES spectra of BaFeO$_3$ thin film grown on SrTiO$_3$ substrate (middle) compared with that of SrFeO$_3$ thin film on LSAT substrate (top) and CI cluster-model calculation (bottom). The vertical bars under the bottom spectrum indicates the calculated states obtained by the CI cluster-model calculations. The states are decomposed into $\underline{c}d^4$, $\underline{c}d^5\underline{L}$ and $\underline{c}d^6\underline{L}^2$ configurations as shown below the spectra. The dotted lines denote the background due to secondary electrons.

TABLE I: Parameters used for the CI Cluster-model calculations of HAXPES in Fig. 1 and Fig. 2, and XAS and XMCD spectra in Fig. 3. See text for details.

	Δ	$(pd\sigma)$	U_{dd}	[eV]
BaFeO$_3$	-0.9	-1.5	7.1	

III. RESULTS AND DISCUSSION

Figure 1 shows the Fe $2p$ core-level HAXPES spectra for SrFeO$_3$ (top), BaFeO$_3$ (middle) and CI cluster-model calculation (bottom). The experimental spectra have main peaks (feature A and A$'$) and weak satellite structures (feature B, C, B$'$ and C$'$) for both the $2p_{3/2}$ and $2p_{1/2}$ transition as indicated in the top and middle spectra of Fig. 1. Since Fe^{3+} would greatly enhance the feature C, the weak intensities of the feature C in our results suggest that the formal valence of Fe is not 3+ but 4+ and that both the sample SrFeO$_3$ and BaFeO$_3$ thin films were fully oxidized (probing depth; $\sim$ 5 nm from the surface) [10, 21, 27]. The peaks A and A$'$ of experimental spectra are asymmetric due to the metallic state in SrFeO$_3$ and small band gap in BaFeO$_3$ thin films, which are often called Doniac-Sanjic asymmetric structure. In order to take it into account, we employed Doniac-Sanjic broadening with asymmetric parameter of 0.3 for the cluster-model calculations [28]. The calculated results suggest that the main peaks (A and A$'$) are mainly composed of the $\underline{c}d^6\underline{L}^2$ configuration. The small features B and B$'$ most likely attribute to the small structures from $\underline{c}d^6\underline{L}^2$ and asymmetry of peaks A and A$'$. The satellite structures of C and C$'$ are composed of strongly hybridized states between $\underline{c}d^5\underline{L}$ and $\underline{c}d^6\underline{L}^2$, as shown in the bottom of Fig. 1. The results of the cluster-model calculations did not reproduce the double-peak structures in the experimental main peaks (A and A$'$). We consider

that the double-peak structures in peak A and A′ stem from the non-local screening effect, since these structures were not seen in the result obtained by soft x-ray [10, 29–33].

The structures of the Fe $2p$ core-level of $BaFeO_3$ are quite similar to that of $SrFeO_3$. The slight lowering in the binding energy of feature C in $BaFeO_3$ compared to that in $SrFeO_3$ originates from the reduction of Fe $3d$ - O $2p$ hybridization in $BaFeO_3$ due to the lattice expansion in $BaFeO_3$ following Harrison's rule for $(pd\sigma) \propto R^{-3.5}$ [34].

Figure 2 shows the valence-band HAXPES spectra of $SrFeO_3$ (top) and $BaFeO_3$ (middle) thin films. We also showed the calculated multiplet state for $BaFeO_3$ thin films in the bottom bars. The bottom bars were broadened by a Lorentzian to consider the lifetime broadening of the photohole, and by a Gaussian for the combined effects of the instrumental resolution and the d band dispersion [27]. The broadened spectrum is also shown in the bottom, which nicely reproduces the experimental result of $BaFeO_3$ thin films. Note that we added O $2p$ band, which is assumed to be a Gaussian, to the Fe $3d$ spectrum to calculate the photoemission spectrum. The energy position of O $2p$ band is deduced from the result of local-spin-density-approximation calculations in Ref. [16].

The spectra have three main structures indicated by A, B and C, respectively, besides the Fermi edge in $SrFeO_3$. A large upturn structure, at ~ 10 eV in $BaFeO_3$, is the tail of Ba $5 p_{3/2}$ core-level peak at ~ 11 eV. The inset shows the expanded spectra near E_F to show the Fermi edge in $SrFeO_3$ and does not in $BaFeO_3$. They clearly contrasts insulating $BaFeO_3$ thin films with metallic $SrFeO_3$. These results agree qualitatively with the resistivity measurements [8, 21]. We deduce that $BaFeO_3$ thin film is a p-type semiconductor, because there is finite spectrum intensity just below the E_F, and the band gap is estimated to be ~ 1.8 eV from the optical measurement [21]. Since $SrFeO_3$ has stronger Fe $3d$ - O $2p$ hybridization due to the smaller lattice constant, the structure of feature A shifts toward higher binding energy, and its bandwidth becomes broader, as we will discuss later. These features are reproduced by local-spin-density-approximation calculations in Ref. [16], although they predicted that $BaFeO_3$ becomes half-metallic. The multiplet states calculated by cluster-model calculations were decomposed into d^3, $d^4\underline{L}$ and $d^5\underline{L}^2$ components. The feature B and C in the experimental spectrum for $BaFeO_3$ consist of strongly hybridized states between $d^4\underline{L}$ and $d^5\underline{L}^2$ configurations. The discrete state composing the feature A, which locates the binding energy of ~ 1.8 eV, is created by the strong Fe $3d$ - O $2p$ hybridization. The results of cluster-model calculations showed that the $d^5\underline{L}^2$ configuration dominates at the discrete first ionization state (2 % d^3, 40 % $d^4\underline{L}$, 58 % $d^5\underline{L}^2$), indicating the heavy O $2p$ character at the state. Therefore, the dominant transition from the ground state to first ionization state is $d^5\underline{L} \longrightarrow d^5\underline{L}^2$, indicating the extra oxygen hole in this transition.

The Fe $2p$ XAS (top) and XMCD (bottom) spectra are shown in Fig. 3 (a). The broad $2p_{3/2}$ XAS peak without shoulder structures reflects the heavily mixed state due to the strong hybridization in $BaFeO_3$ which is quite similar to that in $SrFeO_3$ [11]. These broad peaks seen in $BaFeO_3$ and $SrFeO_3$ suggests that the valence of Fe is not 3+ but 4+ [11]. Fe $2p$ XMCD shows a large peak intensity of ~ 18 % of the XAS peak intensity. The XMCD intensity of $BaFeO_3$ thin film is approximately twice as large as that of bulk $BaFeO_3$ [35]. To obtain the orbital moment (M_{orb}) and spin moment (M_{spin}), we applied XMCD sum rules in Eq. (5) and (6) [36, 37].

$$M_{orb} = \frac{2n_h}{3N} \int_{2p_{1/2}+2p_{3/2}} \Delta\mu \ dE \tag{5}$$

$$M_{spin} - \frac{7}{2}M_T = \frac{n_h}{N}\Big(\int_{2p_{3/2}}\Delta\mu \ dE \ - 2\int_{2p_{1/2}}\Delta\mu \ dE\Big) \tag{6}$$

$\Delta\mu = \mu^+ - \mu^-$ and $\frac{1}{2}(\mu^+ + \mu^-)$ corresponds to the XMCD and XAS intensity defining the expression for $N = \frac{1}{2}\int_{2p_{1/2}+2p_{3/2}}(\mu^+ + \mu^-) \ dE$. Here, μ^+ and μ^- denote the absorption intensities for left-handed and right-handed circularly polarized incident photons. n_h denotes the number of holes in the d orbital, and we assumed $n_h = 5$ for this analysis, because of the result of the cluster-model calculations. M_T denotes the z component of the magnetic dipole moment. Given in a cubic field, the finite M_T can be obtained only via spin-orbit coupling. However, the spin-orbit interaction in a $3d$ transition-metal compound is quite small, making M_T sufficiently quenched and negligible with respect to M_{spin} [37–39].

By applying the XMCD sum rules, we obtained a large magnetic moment of $M_{total} = 1.7 \pm 0.2 \, \mu_B/f.u.$, composed of $M_{spin} = 1.5 \pm 0.1 \, \mu_B/f.u.$ and $M_{orb} = 0.2 \pm 0.1 \, \mu_B/f.u.$.

The XMCD sum-rule analyses often underestimate the magnetization because of the strong Coulomb interaction and saturation effects in total-electron-yield method [40, 41]. The strong Coulomb interaction in the final state make it impossible to separate the $2p_{3/2}$ and $2p_{1/2}$ absorption edges, making underestimations in magnetic moment [37, 40]. The saturation effects distorts the absorption spectra especially where the x-ray attenuation length (~ 50 nm) is comparable to the electron escape depth (~ 5 nm), i.e. at the absorption edges. As a result, sum-rule analyses provide underestimated spin and orbital magnetic moment. We considered the correction coefficient of $1/0.58$ for M_{spin} due to strong electronic correlations [40]. We also considered corrections of $1/0.88$ for M_{spin} and $1/0.49$ for M_{orb} to compensate for the saturation effect in total-electron-yield mode [23].
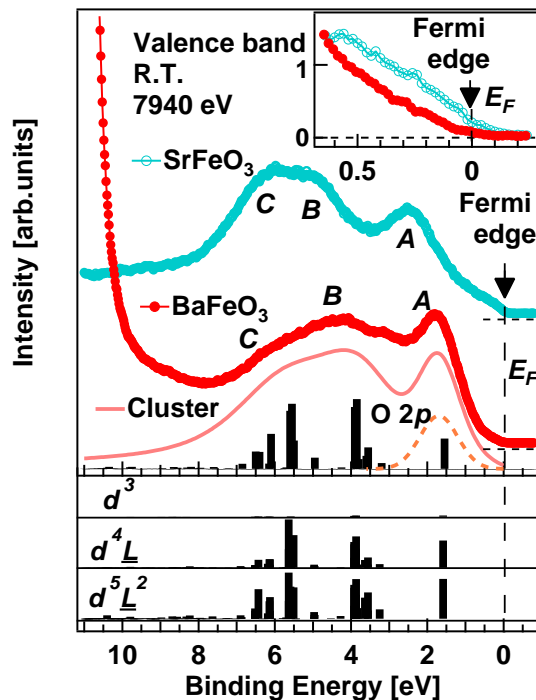
FIG. 2: (Color online) HAXPES valence-band spectra of $SrFeO_3$ (top) and $BaFeO_3$ (middle) thin films. The bottom spectrum is the result of the cluster-model calculations, which the multiplet states, shown as bars below the spectrum, were broadened. The inset shows the expanded spectra around E_F. The multiplet states decomposed into d^3, $d^4\underline{L}$ and $d^5\underline{L}^2$ components are also shown below those spectra.

Since both the M_{spin} (> 0) and M_{orb} (> 0) have the same sign in $BaFeO_3$, it suggests the substantial weight of the $d^6\underline{L}^2$ configuration in the ground state of $BaFeO_3$, by taking Hund's rule into account. Since $BaFeO_3$ thin films have negative charge transfer energy, it is deduced that the $d^6\underline{L}^2$ configuration is stabilized some extent besides the main component of the $d^5\underline{L}$ configuration, which is consistent with the CI cluster-model calculations. The magnetic moment obtained by the experimental XMCD and superconducting quantum interference device (SQUID) measurements are shown in TABLE II. The XMCD result gave a smaller total magnetic moment than the value obtained by SQUID measurement. The origin of the deviation is not clear at this moment, but there is a possibility that the magnetic moment on the oxygen site might cause the underestimation based on the total magnetic moment in the iron site. Another possibility is the surface sensitivity of the total-electron-yield measurement. The probing depth of XAS and XMCD is smaller than the film thickness. There may be possible nonmagnetic surface due to oxygen vacancies, making reduced magnetic moment.

In Fig. 3 (b), the calculated Fe $2p$ XAS (top) and XMCD (bottom) spectra are presented. The cluster-model spectrum reproduces the features of the experimental results very well, as oppose to the atomic multiplet calculation for d^4 in Ref. [11], suggesting the importance of charge transfer effects in this system.

The O $1s$ XAS (top) and XMCD (bottom) spectra are presented in Fig. 4. O $1s$ XAS spectra of correlated compounds originate from transitions into unoccupied states with O $2p$ character hybridized with transition metal $3d$ states. Therefore, the structure of the spectrum is qualitatively related to empty bands of primarily Fe $3d$ weight. The structure from 528 eV to 534 eV, mainly Fe $3d$-related, is similar to that of $SrFeO_3$ [11]. The O $1s$ XAS of $La_{1-x}Sr_xFeO_3$ shows that a new structure below the threshold of $LaFeO_3$ grows rapidly with increasing Sr, and dominates the spectra at high concentrations, corresponding to the Fe related main structure in our spectrum [11]. Those main features seen in $SrFeO_3$ and $BaFeO_3$ are attributed strong hybridization between Fe $3d$ - O $2p$ with $e_{g\uparrow}$ symmetry. Such effective states are also seen in $La_{2-x}Sr_xCuO_4$ and $Li_xNi_{1-x}O$ due to the anomalously strong antiferromagnetic coupling between Cu or Ni $3d$ and O $2p$ [42, 43].

The O $1s$ XMCD spectrum directly shows that the effective state in $BaFeO_3$ has O $2p$ character with the peak intensity of ~ 4 % versus that of XAS. This is the evidence of the significant O $2p$ hole character in the ground states due to the negative charge transfer energy and strong Fe $3d$ - O $2p$ hybridization [41].

Since the threshold of XAS is dominated by the transition of $d^5\underline{L} \longrightarrow \underline{1s}d^5$, the strong intensity of XMCD was
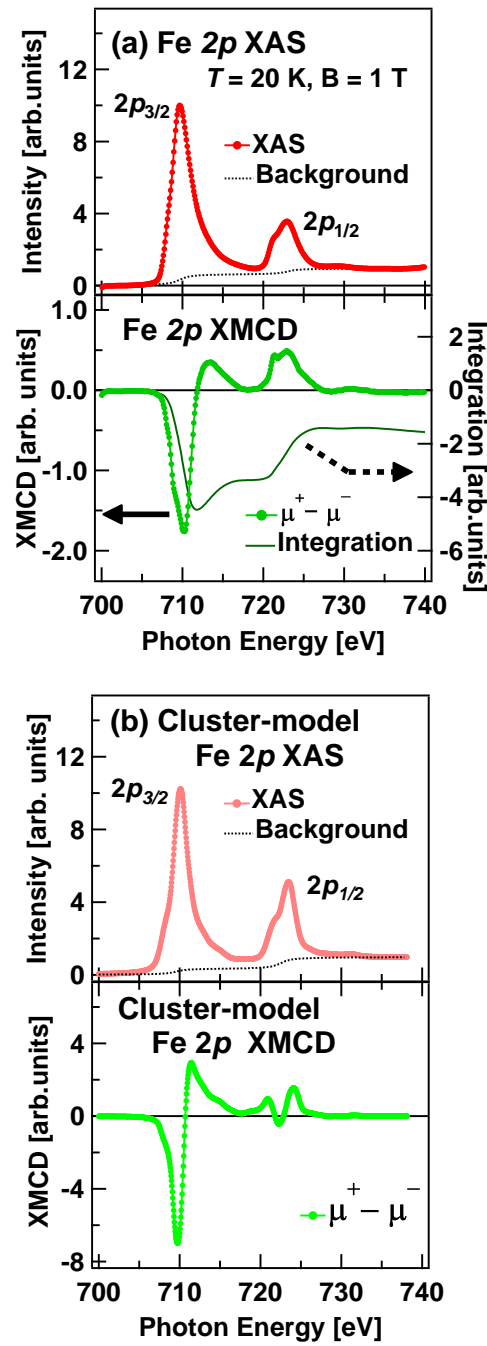
FIG. 3: (Color online) Fe $2p$ XAS and XMCD spectra of BaFeO$_3$ thin films are shown in panels (a) and (b) obtained by experiment and CI cluster-model calculation, respectively.

observed at the XAS structure of the lowest energy even in the usually nonmagnetic oxygen. Here, $\underline{1s}$ denotes the O $1s$ core hole created by the incident x-ray. Thus, when an extra electron is added to the ground state, the electron will be introduced into the ligand hole at the affinity level.

We showed that the experimental spectra of BaFeO$_3$ are reproduced quite well by the results of CI cluster-model calculations with a common set of parameters, which can explain the magnetic ground state of BaFeO$_3$ by comparing to the phase diagram in Ref. [12]. The CI cluster-model calculations clarified that the ground state, the first affinity level and first ionization level are dominated by $d^5\underline{L}$ (17 % d^4, 65 % $d^5\underline{L}$, 18 % $d^6\underline{L}^2$), by d^5 (71 % d^5, 26 % $d^6\underline{L}$, 3 % $d^7\underline{L}^2$) and by $d^5\underline{L}^2$ (2 % d^3, 40 % $d^4\underline{L}$, 58 % $d^5\underline{L}^2$). Therefore, the band gap is characterized by $d^5\underline{L} + d^5\underline{L} \longrightarrow d^5$
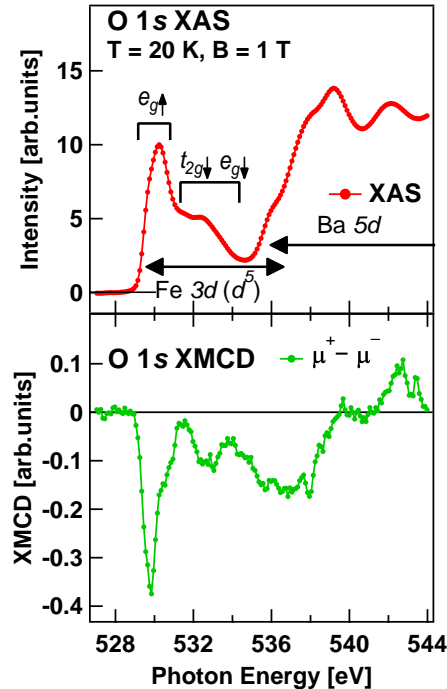
FIG. 4: (Color online) O 1s XAS and XMCD spectra of BaFeO₃ thin films are presented.

TABLE II: Magnetization obtained by XMCD and SQUID. We applied the XMCD sum rules to obtain spin, magnetic and total magnetic moments from Fe 2p XMCD. The SQUID measurement is taken from Ref. [21].

	M_{spin}	M_{orb}	M_{total}	$[\mu_B/f.u.]$
XMCD	1.5 ± 0.1	0.2 ± 0.1	1.7 ± 0.2	
SQUID	—	—	2.7	

+ $d^5\underline{L}^2$ and has significant O 2p character, which is schematically shown in the right panel of Fig. 5 [44]. From those results and the set of the parameters for the CI cluster-model calculation, BaFeO₃ is classified as a covalent insulator (negative-charge-transfer-energy insulator) as proposed by Sarma et al. (Mizokawa et al.) in the modified Zaanen-Sawatzky-Allen diagram. [1, 45–49]. Zaanen-Sawatzky-Allen diagram, which classifies the electronic properties of correlated materials systematically, was modified to consider the insulating phase due to the strong covalency within the negative-charge-transfer-energy region [46–48].

The $d^5\underline{L}$ configuration composing the ground state is originally a continuum and thus it tends to be metallic. The strong Fe 3d - O 2p hybridization, however, creates the $d^5\underline{L}$-like split-off state below the continuum $d^5\underline{L}$ structure with significant stabilization, as schematically shown in the left panel in Fig. 5 [48]. As a result, the oxygen hole is strongly localized despite the weak electronic correlation on the oxygen site.

Due to the localized oxygen hole, the system becomes an insulator and the band gap opens, as shown in the right panel of Fig. 5 [48]. NaCuO₂ (Cu³⁺) has also localized oxygen holes due to anomalously strong antiferromagnetic Cu 3d - O 2p hole coupling, whose split-off $d^9\underline{L}$-like state with the $^1A_1$ symmetry is denoted as the Zhang-Rice singlet [49].

Although the discrete split-off state is stable within a single cluster, the band gap tends to become unstable and collapse in a periodic lattice, unless the interactions between the clusters are weak, such as for the distorted bond angle structure in CaFeO₃, or orthogonality of the orbitals between the clusters in NaCuO₂ [48]. However, the small band gap in CaFeO₃ by small distortions, unlike the strong one in NaCuO₂, induces charge disproportionation by overcoming the band gap of $d^5\underline{L} + d^5\underline{L} \longrightarrow d^5 + d^5\underline{L}^2$ [3, 48]. On the other hand, the non-distorted structure in SrFeO₃, with the Fe-O-Fe bond angle of ∼ 180°, completely closes the band gap to form a metal in a periodic lattice. According to the modified Zaanen-Sawatzky-Allen diagram, the boundary of the metal-insulator transition is sensitive
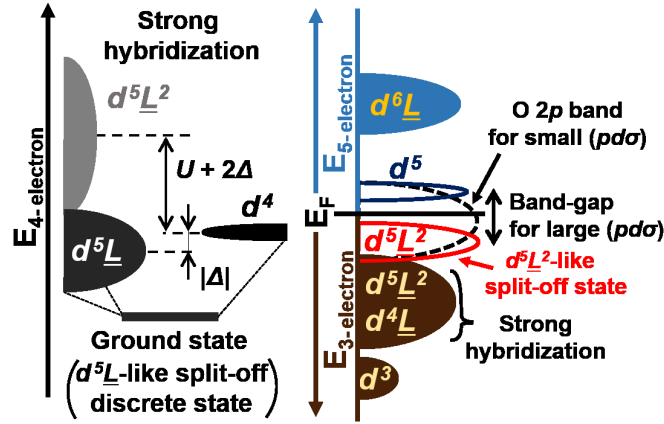
FIG. 5: (Color online) Energy levels for the 4-electron system (left) and the density of states for $BaFeO_3$ are schematically shown (right panel). Due to the strong Fe $3d$ - O $2p$ hybridization, the $d^5\underline{L}$-like split-off state is created under the continuum $d^5\underline{L}$ state (left panel). As a result, the band gap of $d^5 + d^5\underline{L}^2$ is formed (right panel) due to the significant stabilization of the discrete state (left panel).

not only to Δ and U, but also $(pd\sigma)$ and O $2p$ bandwidth denoted by W_p, within the negative-charge-transfer-energy regime [46–48]. In this regime, the band gap tends to be larger as $(pd\sigma)$ increases and as W_p decreases [48].

In the case of $BaFeO_3$ and $SrFeO_3$, the metal-insulator transition occurs due to the competition of the parameters of $(pd\sigma)$ and W_p. We should note that the effective one-electron bandwidth is approximately related to $(pd\sigma)$ by $W_p \propto (pd\sigma)^2$ via the second-order process. Since the ratio of atomic distances in $BaFeO_3$ to $SrFeO_3$ is $\left(\dfrac{R_{BFO}}{R_{SFO}}\right) \sim 1.03$, we obtained the rough estimation of the ratio of $\dfrac{(pd\sigma)_{BFO}}{(pd\sigma)_{SFO}} \sim \left(\dfrac{R_{BFO}}{R_{SFO}}\right)^{-3.5} \sim 0.91$ and of $\dfrac{(W_p)_{BFO}}{(W_p)_{SFO}} \sim \left(\dfrac{R_{BFO}}{R_{SFO}}\right)^{-7} \sim 0.82$, from Harrison's rule [34]. The band gap in $BaFeO_3$ is explained by the significant reduction of the bandwidth compared to the relatively weaker reduction of the Fe $3d$ - O $2p$ hybridization. We can see directly the differences of those parameters in their valence-band spectra in Fig. 2. The feature A of $SrFeO_3$ is located at a higher binding-energy position than that of $BaFeO_3$. Since the Fe $3d$ - O $2p$ hybridization is stronger in $SrFeO_3$, the split-off discrete state of 4-electron systems (see left panel in Fig. 5) is more stable than that of $BaFeO_3$. As a result, the energy difference of the ground state in 4-electron systems and feature A in 3-electron systems for $SrFeO_3$ tends to be larger than that for $BaFeO_3$. The broader bandwidth of feature A in $SrFeO_3$ valence-band spectrum compared to that in $BaFeO_3$ also suggests the stronger Fe $3d$ - O $2p$ hybridization in $SrFeO_3$. Even in the non-distorted structure in $BaFeO_3$ and in a periodic lattice, the band gap remains open since the interactions between the clusters are weak due to the larger lattice constant.

To summarize, as the lattice constant increases from $CaFeO_3$ to $SrFeO_3$, the Fe-O-Fe bond angle straightens to $\sim 180°$ and the O $2p$ bandwidth increases. Therefore, $SrFeO_3$ is metallic. When the lattice constant is further increased from $SrFeO_3$ to $BaFeO_3$ the effect of narrowing bandwidth causes a further transition to an insulator.

The coefficient of antiferromagnetic superexchange interaction (J) greatly reduces as the lattice constant increases. By considering Harrison's rule, we can roughly estimate the ratio of J between $BaFeO_3$ and $SrFeO_3$ as $\sim \dfrac{(J)_{BFO}}{(J)_{SFO}} \sim \left(\dfrac{R_{BFO}}{R_{SFO}}\right)^{-14} \sim 0.67$ [34]. This reduction of J in $BaFeO_3$ induces stabilization of ferromagnetic or A-type helicoidal magnetic phases, compared to $SrFeO_3$ [12]. Mostovoy explained that the ferromagnetic phase in Fe^{4+} perovskite crystal structure with negative charge transfer energy is unstable, due to the high density of spin-flip excitations of holes from the spin-down Fermi-sea to pure oxygen spin-up bands [12]. On the other hand, if the spin-flip excitation is suppressed by opening a band gap in the insulating phase, the ferromagnetic phase can be stable. Thus, the reduction of antiferromagnetic superexchange interaction and the insulating phase of $BaFeO_3$ together stabilize the ferromagnetic phase.

IV. CONCLUSION

We investigated the electronic and magnetic properties of BaFeO$_3$ thin films by HAXPES, XAS, XMCD and CI cluster-model analysis. We employed the parameters for CI cluster-model calculations on the phase boundary of ferromagnetic and A-type helicoidal magnetic phase in order to explain the magnetic properties of BaFeO$_3$. The calculated results reproduced all of the experimental spectra quite well. The CI cluster-model calculation suggests that BaFeO$_3$ thin film has negative charge transfer energy, and its ground state is dominated by the $d^5\underline{L}$ electronic configuration. The valence-band HAXPES showed the insulating property of BaFeO$_3$ thin films. The band gap has heavy O $2p$ character, suggesting that BaFeO$_3$ is a covalent insulator. We obtained the saturation magnetic moment of $1.7 \pm 0.2\,\mu_B/f.u.$ from Fe $2p$ XMCD and found that it is composed of large spin magnetic moment and small orbital magnetic moment. Such a stable ferromagnetic phase under small magnetic field derives from the reduction of the antiferromagnetic superexchange interaction and the suppression of the spin-flip excitation due to the band gap in BaFeO$_3$ thin films. Thus, the metal-insulator transition and magnetic phase transition between SrFeO$_3$ and BaFeO$_3$ derive from the difference of their lattice constants, and the resultant bandwidth tuning

[1] M. Imada, A. Fujimori, and Y. Tokura, Rev. Mod. Phys. **70**, 1039 (1998).
[2] M. Takano, and Y. Takeda, Bull. Inst. Chem. Res. Kyoto Univ. **61**, 406 (1983).
[3] T. Akao, Y. Azuma, M. Usuda, Y. Nishihata, J. Mizuki, N. Hamada, N. Hayashi, T. Terashima, and M. Takano, Phys. Rev. Lett. **91**, 156405 (2003).
[4] P. M. Woodward, D. E. Cox, E. Moshopoulou, A. W. Sleight, and S. Morimoto, Phys. Rev. B **62**, 844 (2000).
[5] Shankar Ghosh, N. Kamaraju, M. Seto, A. Fujimori, Y. Takeda, S. Ishiwata, S. Kawasaki, M. Azuma, M. Takano, and A. K. Sood, Phys. Rev. B **71**, 245110 (2005).
[6] M. Reehuis, C. Ulrich, A. Maljuk, C. Niedermayer, B. Ouladdiaf, A. Hoser, T. Hofmann, and B. Keimer, Phys. Rev. B **85**, 184109 (2012).
[7] S. Ishiwata, M. Tokunaga,Y. Kaneko, D. Okuyama, Y. Tokunaga, S. Wakimoto, K. Kakurai, T. Arima, Y. Taguchi, and Y. Tokura, Phys. Rev. B **84**, 054427 (2011).
[8] S. Chakraverty, T. Matsuda, H. Wadati, J. Okamoto, Y. Yamasaki, H. Nakao, Y. Murakami, S. Ishiwata, M. Kawasaki, Y. Taguchi, Y. Tokura, and H. Y. Hwang, Phys. Rev. B **88**, 220405(R) (2013).
[9] N. Hayashi, T. Terashima, and M. Takano, J. Mater. Chem. **11**, 2235 (2001).
[10] A. E. Bocquet, A. Fujimori, T. Mizokawa, T. Saitoh, H. Namatame, S. Suga, N. Kimizuka, Y. Takeda, and M. Takano, Phys. Rev. B **45**, 1561 (1992).
[11] M. Abbate, F. M. F. de Groot, J. C. Fuggle, A. Fujimori, O. Strebel, F. Lopez, M. Domke, G. Kaindl, G. A. Sawatzky, M. Takano, Y. Takeda, H. Eisaki, and S. Uchida, Phys. Rev. B **46**, 4511 (1992).
[12] M. Mostovoy, Phys. Rev. Lett. **94**, 137205 (2005).
[13] J. Zaanen, G. A. Sawatzky, and J. W. Allen, Phys. Rev Lett. **55**, 418 (1985).
[14] N. Hayashi, T. Yamamoto, H. Kageyama, M. Nishi, Y. Watanabe, T.Kawakami, Y. Matsushita, A. Fujimori, and M. Takano. Angew. Chem. Int. Ed. **50**, 12547 (2011).
[15] Z. Li, R. Laskowski, T. Iitaka, and T. Tohyama, Phys. Rev. B **85**, 134419 (2012).
[16] Z. Li, T. Iitaka, and T. Tohyama, Phys. Rev. B **86**, 094422 (2012).
[17] T. Matsui, H. Tanaka, N. Fujimura, T. Ito, H.Mabuchi, and K. Morii, Appl. Phys. Lett. **81**, 2764 (2002).
[18] C. Callender, D. P. Norton, R. Das, A. F. Hebard, and J. D. Budai, Appl. Phys. Lett. **92**, 012514 (2008).
[19] E. Taketani, T. Matsui, N. Fujimura, and K. Morii, IEEE Trans. Magn. **40**, 2736 (2004).
[20] B. Ribeiro, R. P. Borges, R. C. da Silva, N. Franco, P. Ferreira, E. Alves, B. Berini, A. Fouchet, N. Keller, and M. Godinho, J. Appl. Phys. **111**, 113923 (2012).
[21] S. Chakraverty, T. Matsuda, N. Ogawa, H. Wadati, E. Ikenaga, M. Kawasaki, Y. Tokura, and H. Y. Hwang, Appl. Phys. Lett. **103**, 142416 (2013).
[22] K. Kobayashi, Nucl. Instrum. Methods A **601**, 32 (2009).
[23] R. Nakajima, J. Stohr, and Y. U. Idzerda, Phys. Rev. B **59**, 6421 (1999).
[24] M. Abbate, J. B. Goedkoop, F. M. F. de Groot, M. Grionit, J. C. Fuggle, S. Hofmann, H. Petersen, and M. Sacchi, Surf. Interface Anal. **18**, 65 (1992).

[25] F. M. F. de Groot, and A. Kotani, *Core Level Spectroscopy in Solids*, CRC press, (2008).

[26] A. Tanaka, and T. Jo, J. Phys. Soc. Jpn, **63**, 2788, (1994).

[27] H. Wadati, D. Kobayashi, H. Kumigashira, K. Okazaki, T. Mizokawa, A. Fujimori, K. Horiba, M. Oshima, N. Hamada, M. Lippmaa, M. Kawasaki, and H. Koinuma, Phys. Rev. B **71**, 035108 (2005).

[28] S. Hüfner, *Photoelectron Spectroscopy: Principles and Applications*, Springer, (2003).

[29] K. Horiba, M. Taguchi, A. Chainani, Y. Takata, E. Ikenaga, D. Miwa, Y. Nishino, K. Tamasaku, M. Awaji, A. Takeuchi, M. Yabashi, H. Namatame, M. Taniguchi, H. Kumigashira, M. Oshima, M. Lippmaa, M. Kawasaki, H. Koinuma, K. Kobayashi, T. Ishikawa, and S. Shin, Phys. Rev. Lett. **93**, 236401 (2004).

[30] M. Taguchi, A. Chainani, K. Horiba, Y. Takata, M. Yabashi, K. Tamasaku, Y. Nishino, D. Miwa, T. Ishikawa, T. Takeuchi, K. Yamamoto, M. Matsunami, S. Shin, T. Yokoya, E. Ikenaga, K. Kobayashi, T. Mochiku, K. Hirata, J. Hori, K. Ishii, F. Nakamura, and T. Suzuki, Phys. Rev. Lett. **95**, 177002 (2005).

[31] M. Taguchi, M. Matsunami, Y. Ishida, R. Eguchi, A. Chainani, Y. Takata, M. Yabashi, K. Tamasaku, Y. Nishino, T. Ishikawa, Y. Senba, H. Ohashi, and S. Shin, Phys. Rev. Lett. **100**, 206401 (2008).

[32] M . A. van Veenendaal, and G. A. Sawatzky, Phys. Rev. Lett. **70**, 2459 (1993).

[33] A. E. Bocquet, T. Mizokawa, A. Fujimori, M. Matoba, and S. Anzai, Phys. Rev. B. **52**, 13838 (1995).

[34] W. A. Harrison, *Electronic Structure and the Properties of Solids, Dover*, New York, (1989).

[35] M. Mizumaki, K. Yoshii, N. Hayashi, T. Saito, Y. Shimakawa, and M. Takano, J. Appl. Phys. **114**, 073901 (2013).

[36] B. T. Thole, P. Carra. F. Sette, and G. van der Laan, Phys. Rev. Lett. **68**, 1943 (1992).

[37] P. Carra, B. T. Thole, M. Altarelli, and X. Wang, Phys. Rev. Lett. **70**, 694 (1993).

[38] R. D. Cowan, The Theory of Atomic Structure, and Spectra (Univ. of California Press, Berkeley, 1981).

[39] J. Stöhr, and H. König, Phys. Rev. Lett. **75**, 3748 (1995).

[40] Y. Teramura, A. Tanaka, and T. Jo, J. Phys. Soc. Jpn. **65**, 1053 (1996).

[41] T. Koide, H. Miyauchi, J. Okamoto, T. Shidara, T. Sekine, T. Saitoh, A. Fujimori, H. Fukutani, M. Takano, and Y. Takeda, Phys. Rev. Lett. **87**, 246404 (2001).

[42] C. T. Chen, F. Sette, Y. Ma, M. S. Hybertsen, E. B. Stechel, W. M. C. Foulkes, M. Schluter, S-W. Cheong, A. S. Cooper, L. W. Rupp, Jr., B. Batlogg, Y. L. Soo, Z. H. Ming, A. Krol, and Y. H. Kao, Phys. Rev. Lett. **66**, 104 (1991).

[43] P. Kuiper, G. Kruizinga, J. Ghijsen, G. A. Sawatzky, and H. Verweij, Phys. Rev. Lett. **62**, 221 (1989).

[44] H. Wadati, A. Chikamatsu, M. Takizawa, H. Kumigashira, T. Yoshida, T. Mizokawa, A. Fujimori, M. Oshima, and N Hamada, J. Phys. Soc. Jpn. **78**, 094709 (2009).

[45] D. D. Sarma, J. Sol. St. Chem. **88**, 45 (1990).

[46] Seva Nimkar, D. D. Sarma, H. R. Krishnamurthy, and S. Ramasesha, Phys. Rev. B **48**, 7355 (1993).

[47] D. D. Sarma, H. R. Krishnamurthy, Seva Nimkar, S. Ramasesha, P. P. Mitra, and T. V. Ramakrishnan, Pramana - J. Phys. **38**, L531 (1992).

[48] T. Mizokawa, A. Fujimori, H. Namatame ,K. Akeyama, and N. Kosugi, Phys. Rev. B **49**, 7193 (1994).

[49] T. Mizokawa, H. Namatame, A. Fujimori, K. Akeyama, H. Kondoh, H. Kuroda, and N. Kosugi, Phys. Rev. Lett. **67**, 1638 (1991).